Circularly-polarised end-fire antenna and arrays for 5G millimetre-wave beam-steering systems

Khaled Al-Amoodi, Mohammad Mahdi Honari, Rashid Mirzavand, Jordan Melzer, Duncan G. Elliott, Pedram Mousavi

Al-Amoodi, Khaled; Honari, Mohammad Mahdi; Mirzavand, Rashid; Melzer, Jordan; Elliott, Duncan G.; Mousavi, Pedram: 'Circularly-polarised end-fire antenna and arrays for 5G millimetre-wave beam-steering systems', IET Microwaves, Antennas & Propagation, 2020, 14, (9), p. 980-987, DOI: 10.1049/iet-map.2019.1119

IET Digital Library, https://digital-library.theiet.org/content/journals/10.1049/iet-map.2019.1119

IET Microwaves, Antennas & Propagation

Research Article

IET Journals
The Institution of Engineering and Technology

Circularly-polarised end-fire antenna and arrays for 5G millimetre-wave beam-steering systems

ISSN 1751-8725
Received on 14th December 2019
Revised 9th April 2020
Accepted on 16th April 2020
doi: 10.1049/iet-map.2019.1119
www.ietdl.org

Khaled Al-Amoodi[1] ✉, Mohammad Mahdi Honari[1], Rashid Mirzavand[1], Jordan Melzer[2], Duncan G. Elliott[1], Pedram Mousavi[1]

[1]*Department of Electrical and Computer Engineering, University of Alberta, Edmonton AB T6G 1H9, Canada*
[2]*Telus Communications, Ottawa ON K1P 0A6, Canada*
✉ *E-mail: kalamood@ualberta.ca*

Abstract: This study presents a circularly-polarised substrate-integrated waveguide end-fire antenna and four-antenna arrays for 5G beam-steering mobile devices at 28 GHz. Polarisation is achieved through implementation of a substrate-integrated waveguide notched-septum polariser. It is then loaded with a dielectric lens to improve gain, axial ratio bandwidth, and circular polarisation (CP) purity. To suppress the mutual coupling between array elements, vias are extended on either side of the lens. It also improves the single-element axial ratio and front-to-back ratio. The antenna's performance is found to be resilient to typical manufacturing tolerances for the lens and via extensions. The element and arrays are manufactured and measured. The prototypes demonstrated an impedance bandwidth of 11.4% with a maximum array gain of 10.5 dBi and a steering range of up to $\pm 35°$ (with reduced performance when steered to $\pm 45°$). Within this range, the antenna array demonstrates a gain variation of up to 3 dB and very good CP purity within the radiation half-power beamwidths (HPBWs). A wide single-element elevation HPBW of $95°$ is also demonstrated. Given its performance and ease of manufacture in a printed circuit board process, the proposed antenna could be a strong candidate for 5G millimetre-wave beam-steering systems.

1 Introduction

The proliferation of highly demanding services (such as high-quality video streaming) and limited network capacities has led to considerable interest in the next generation of mobile communication (5G) [1, 2], with a focus on operating in higher frequency bands around 28 and 38 GHz [3–5]. Research is proposing different arrays of end-fire antennas for fan-beam patterns [6–8]. These can be implemented on all edges of a mobile terminal and used in conjunction with planar antennas to give full coverage around the device. The appropriate arrays can be selected and then steered. Several end-fire antenna arrays have been proposed: dielectric-embedded dipoles [9, 10], magnetoelectric-dipoles [11], mesh-grid patches [12], antipodal antennas [13], and substrate-integrated waveguide (SIW) based [14]. These arrays, however, have certain limitations: sensitivity to misalignment in operation or lack of robustness to variations in manufacturing. The antennas should be capable of more than just a linear polarisation, for greater channel robustness through polarisation diversity as proposed in [15–17]. Circular polarisation (CP) is thus a necessity to limit polarisation loss. As for robustness to manufacturing variation, given the high frequency of operation, any variation in dimensions or dielectric properties will manifest in poorer gain, patterns, impedance bandwidth, and axial ratio bandwidth.

To address the problems and requirements above, this study presents a SIW-based antenna, with a notched-septum polariser for CP generation, dielectric lens for improved radiation and axial ratio performance, and via extensions alongside the lens for coupling-suppression, improved front-to-back ratio, and axial ratio. Effects on performance from manufacturing variations of the lens and via extensions are also investigated. Four 4×1 arrays with a feeding network and passive phase shifters are also designed and manufactured to investigate the steering capability of the antenna and its prospective use in beam-steering CP end-fire arrays.

This paper is organised as follows. The antenna element design, evolution, and operation principle are described in Section 2. Parametric studies are discussed in Section 3. In Section 4, arrays of four elements of the aforementioned antennas are designed, followed by experimental results of the single-element antenna and arrays in Section 5. Finally, this paper is concluded in Section 6.

2 Antenna element design

The final structure of the single antenna element is shown in Fig. 1 and associated dimensions are listed in Table 1. The element is implemented with Rogers RO4350B substrates ($\epsilon_r = 3.66$ and $\tan\delta = 0.0037$) with a total thickness of 3.7 mm. The structure consists of two SIWs stacked on top of each other with a shared broad wall. The shared wall ends as a notched-septum polariser for circular-polarisation generation. While the two rectangular SIW ports can be fed individually (for left-handed or right-handed CPs), only the top one is used. On the other end, where the broad wall ends in the polariser, the waveguides fuse and form a square waveguide (port 3) to propagate both first transverse electric modes. The dielectric lens matches the SIW to air and also frequency shifts the axial ratio bandwidth. The via extensions on either side of the lens act as horns and also coupling-reduction mechanisms in array configurations. The antenna is oriented in the x–y (azimuth) plane, pointing towards 0° (+x-axis), as shown in Fig. 1*a*. The elevation plane is perpendicular to the azimuth, with 0° being at the +z axis. The antenna element design evolved in the three stages shown in Fig. 2. At each step, performance is observed through three metrics: impedance matching, radiation patterns, and axial ratio. To ensure that simulation results are measurement-relevant later, a transition from grounded coplanar waveguide (GCPW) to SIW [18] and an subminiature push-on (SMP) connector are implemented at port 1 in the simulation models.

The design process begins with the choice of the polarisation mechanism. Rather than using multiple elements of orthogonal polarisations (such as in [15, 19, 20]), the single antenna element will incorporate the polarisation mechanism within it (similar to [21]), thus making the structure compact. Specifically, it is a SIW notched-septum polariser. While notched-septum polarisers achieve narrower axial ratio bandwidths than other septum polarisers [22–24], they are smaller in length and are thus more suitable for mobile devices. While other waveguide polarisers exist, they have not seen implementations in SIW due to

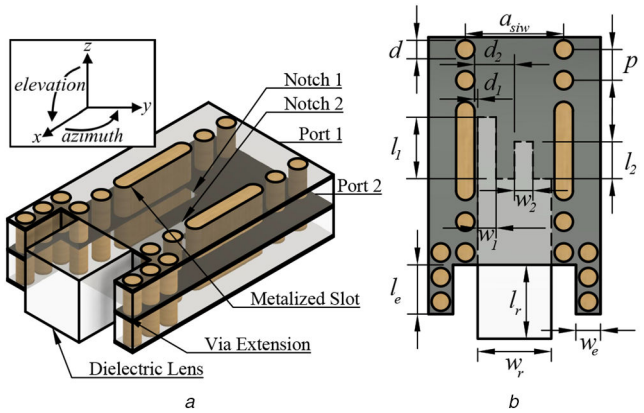

Fig. 1 *Structure of the open-ended SIW antenna with integrated polariser* ***(a)*** Isometric view, ***(b)*** Top view

Table 1 Parameters of the single antenna element

Parameter	Dimension
a_{siw}	4.50
d	1.00
p	1.20
l_e	2.50
w_e	1.80
l_r	3.60
w_r	3.60
l_1	1.45
w_1	0.15
d_1	0.18
l_2	1.32
w_2	0.30
d_2	2.03

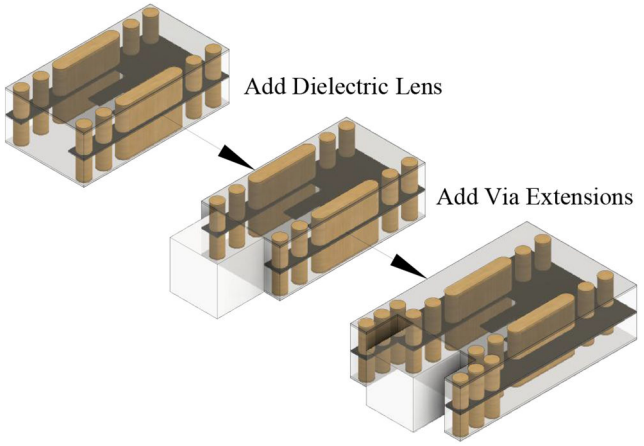

Fig. 2 *Design stages of the SIW antenna element with integrated polariser*

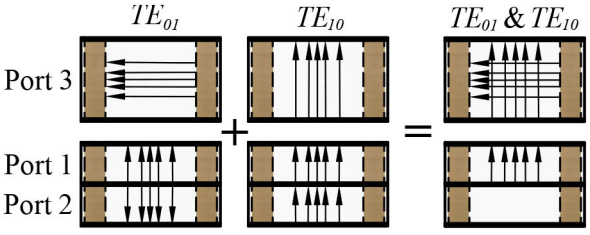

Fig. 3 *Operation of the SIW notched-septum polariser for horizontal, vertical, and right-handed CPs*

manufacturing complexity [25, 26]. Fig. 3 illustrates the operation of the polariser. Ports 1 and 2 are designed to only guide the TE_{10} mode, whereas port 3 is designed to guide both TE_{10} and TE_{01}. Vertical fields are achieved at port 3 by exciting ports 1 and 2 with equal amplitude, but 180° phase difference. Similarly, horizontal fields are achieved at port 3 by exciting ports 1 and 2 with equal amplitude and phase. The horizontal fields also demonstrate 90° phase offset from the vertical fields from the previously-mentioned method of operation. Given that a CP is a combination of vertical and horizontal polarizations with 90° phase offset, a right-handed CP from port 3 can be achieved by combining the two previous methods of operation, i.e. by only exciting port 1. Fig. 4 shows the simulated performance of the antenna at this step. A wide impedance matching bandwidth is observed, and the 3 dB axial ratio bandwidth is observed to be 1 GHz, centred at 28.5 GHz.

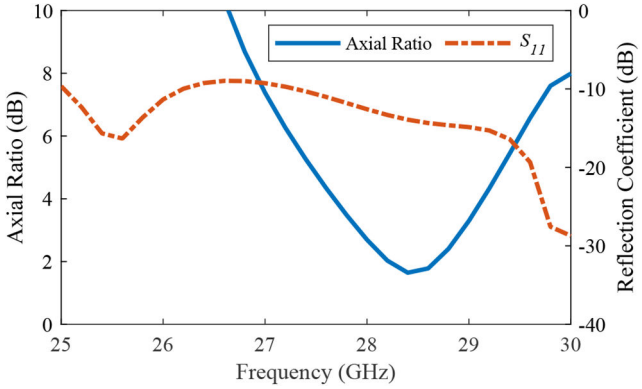

Fig. 4 *Simulated reflection coefficient and axial ratio (versus frequency) of a SIW notched-septum polariser*

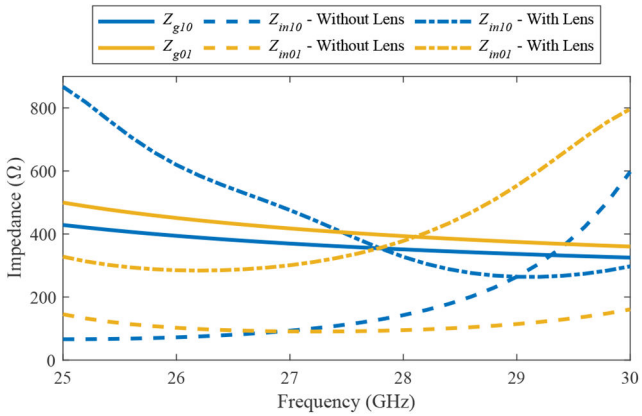

Fig. 5 *Simulated input impedances (Z_{in10} and Z_{in01}) of the radiator with and without a dielectric lens, and square SIW guided waves' impedances (Z_{g10} and Z_{g01})*

Fig. 5 presents (for the TE_{10} and TE_{01} modes) the open-ended SIW input impedance in relation to the guided wave impedances of the square SIW (following the polariser). The guided wave impedance is dependent on the dielectric material and SIW width as demonstrated in the following equation:

$$Z_g = \frac{Z_o}{\sqrt{\epsilon_r - \left(\frac{c}{2 \cdot a_d \cdot f}\right)^2}} \quad (1)$$

where Z_g is the guided wave impedance, Z_o is the free space impedance, c is the speed of light in free space, f is the frequency and a_d is the effective dielectric-filled waveguide width. For the TE_{01} mode, given that in that orientation the side walls are continuous metallic walls, a_d is the total structure thickness. For the TE_{10} mode, however, the side walls are implemented as vias and a_d is calculated using [27]

$$a_d = a_{SIW} - \frac{d^2}{0.95 \cdot p} \quad (2)$$

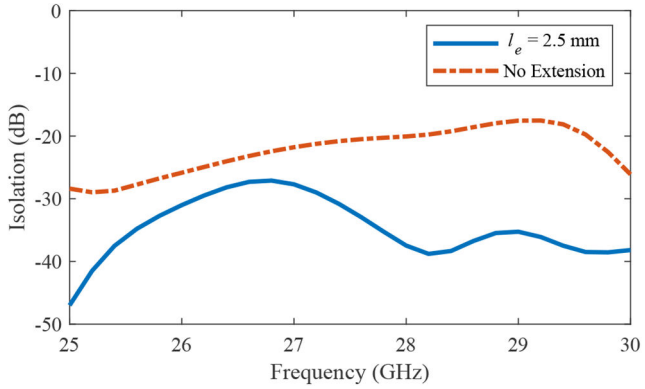

Fig. 6 *Simulated isolation between two elements in an array with no via extension and with via extensions of l_e of 2.5 mm*

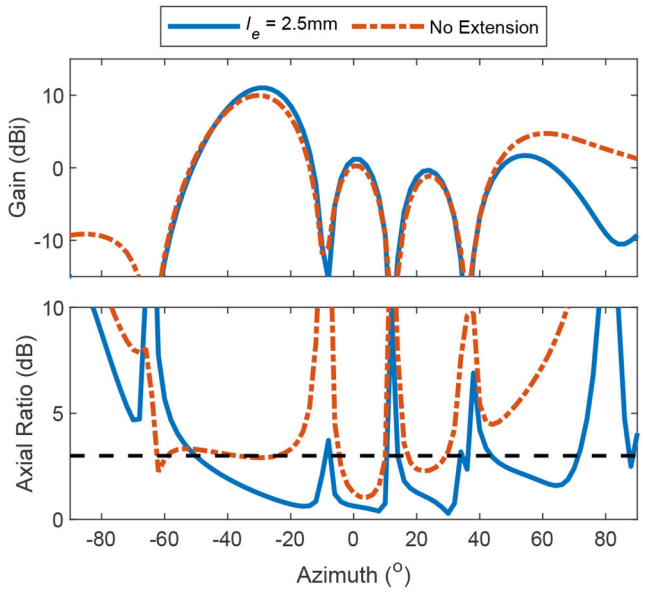

Fig. 7 *Simulated azimuth gain and axial ratio of four-element arrays with no via extension and with via extensions of l_e of 2.5 mm, with ports fed appropriately for an RHCP beam at −30°*

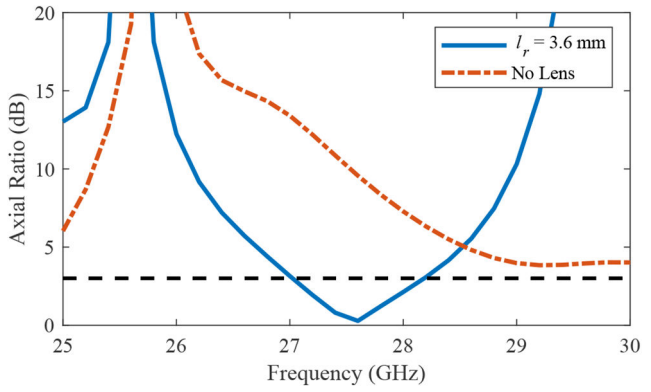

Fig. 8 *Simulated boresight axial ratios of a single-element antenna with no lens and with a lens length of l_r of 3.6 mm*

where a_{SIW} is the SIW width, d is the SIW vias diameter and p is the SIW vias pitch, with all three dimensions as labelled in Fig. 1. While the SIW was designed such that the effective width would be identical to its thickness, there is a sufficient enough difference to result in a difference in guided wave impedance between the two modes, as seen in Fig. 5. For best power transfer and radiation, there must be matching between the radiator input impedance and the guided wave impedance of the two modes within the square SIW. It is evident that this is not the case for the open-ended SIW radiator. Flaring horn antennas [28] are not suitable radiation mechanisms for our application due to the narrow resultant radiation patterns (thus smaller array steering range) and increased element size. Several otherwise viable structures are not chosen given their manufacturing complexity [29–32]. Instead, a dielectric lens [33] is added to port 3 of the polariser. In Fig. 5, the input impedances of the dielectric lens radiator are also shown. It is observed that by extending the dielectric beyond the SIW into a lens, the two modes' input impedances are increased sufficiently to be within the close agreement to the guided wave impedances within our band of interest, resulting in a better gain. Furthermore, given that the individual modes' input impedances are identically close to their respective guided wave impedances, the individual modes are similarly matched, thus the radiated axial ratio would be similar to that observed in the polariser structure.

While the single element after the previous step is sufficient as a stand-alone antenna, its use in an array is limited due to mutual coupling between adjacent elements. This coupling results in poorer axial ratio performance. Thus, the next step is to improve the element's performance within an array. Via extensions (as straight horns) are introduced to suppress the surface waves from propagating to nearby elements. Fig. 6 shows simulated isolation performance for an array of two elements. It demonstrates that the use of the via extensions results in 20 dB better isolation between the two elements. The improved isolation between elements results in significantly improved CP purity and reduced sidelobe levels. These improvements are demonstrated in Fig. 7, which presents the simulated azimuth gain and axial ratio of four-element arrays with appropriate feed amplitudes and phases for a right-handed CP (RHCP) beam at −30°. One array has no via extension, whereas the other has via extensions of the nominal length l_e of 2.5 mm. We also demonstrate in Section 3 that the via extensions improve single-element antenna performance: the front-to-back ratio (due to the extensions acting as a horn) and axial ratio.

3 Parametric study

In this section, parametric studies are conducted to examine and better understand the influence of several design dimensions on the antenna's performance. Specifically, the dielectric lens length (l_r) and via extensions' length (l_e) are examined. The effects of the parameters on the reflection coefficient, axial ratio, and gain are studied. During each study, only one parameter is swept while the others remain nominal (as given in Table 1).

3.1 Dielectric lens

Fig. 8 shows the axial ratio versus frequency for the antenna with and without a lens. A shift in the axial ratio is observed when the lens is added, allowing it to be used as a mechanism to fine-tune the band of operation (to account for variations in ϵ_r or manufacturing). Thus, a parametric study is conducted on the lens length (l_r) with values beyond 2.8 mm ($\lambda_d/2$ at 28 GHz, where λ_d is the wavelength within the dielectric). Fig. 9 shows reflection coefficient simulation results for l_r from 0 to 4.8 mm. Impedance matching improves with increasing l_r, but plateaus beyond 3 mm. The absence of a lens demonstrates poor matching. As shown in Fig. 10, with an increase in l_r, the antenna gain increases due to the effect of the dielectric lens. As was the case with impedance matching, only small improvement is seen beyond 3.5 mm. It is also observed in Fig. 10 that increasing l_r up to 3.6 mm results in better axial ratio. However, the deviation in l_r beyond that results in poorer axial ratio performance. It can be seen that considering typical printed circuit board (PCB) manufacturing tolerance of ±0.2 mm for the lens length l_r, only minimal variation in gain and axial ratio performance would be seen.

3.2 Via extensions

The via extensions are crucial in reducing coupling between adjacent elements. To find out the effects of this parameter on the single-element antenna's radiation performance, a parametric study is performed. The via extensions' length (l_e) is swept from 0 mm

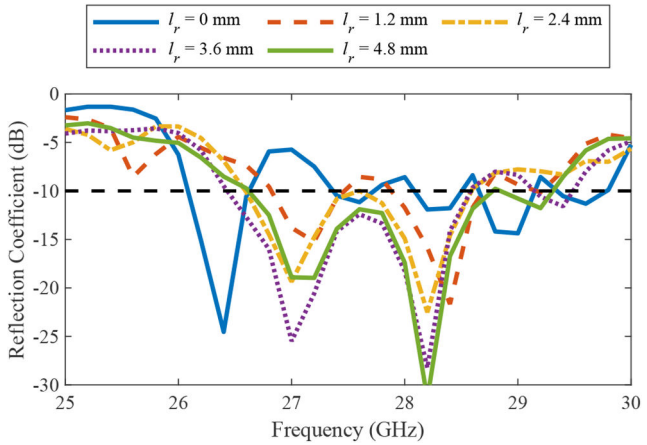

Fig. 9 *Simulated reflection coefficients of a single-element antenna for different lens lengths* l_r *(in mm)*

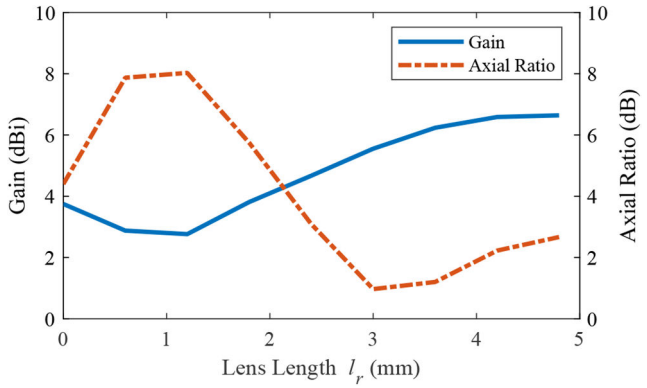

Fig. 10 *Simulated gain and axial ratio of a single-element antenna versus lens lengths* l_r *(in mm)*

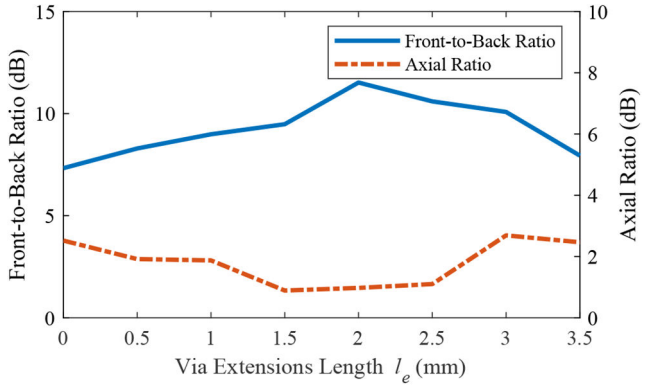

Fig. 11 *Simulated front-to-back ratio and axial ratio of a single-element antenna versus via extensions lengths* l_e *(in mm) at 28 GHz*

(i.e. no extension) up to 3.5 mm. This is to sweep over a decent range around the initial assumption of 2.7 mm ($\lambda_o/4$ at 28 GHz, where λ_o is free-space wavelength). Fig. 11 shows that the axial ratio performance is best for l_e of 2.5 mm. It also demonstrates the simulated front-to-back ratio at 28 GHz, with performance peaking for l_e of 2 mm. Thus, while its intended purpose was to improve axial ratio performance within an array, it also improves single element radiation and axial ratio performances. Furthermore, given the typical tolerance of ±0.2 mm, it is seen that such a variation in l_e would not result in a measurable difference in performance. This parameter, however, does not affect the reflection coefficient much. Just as for the dielectric lens, the use of the via extensions resulted in a wider axial ratio bandwidth, better axial ratio within its respective bandwidth and a shift to a lower frequency.

4 Four-element linear arrays

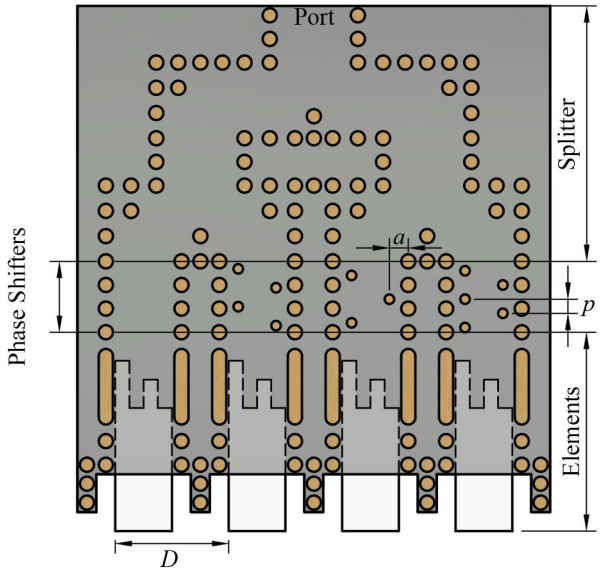

Fig. 12 *General structure of the four-element linear arrays*

Table 2 Parameter values for each fixed phase shifter

	Element 1			Element 2			Element 3			Element 4		
Angle	*a*, mm	*p*, mm	*n*	*a*, mm	*p*, mm	*n*	*a*, mm	*p*, mm	*n*	*a*, mm	*p*, mm	*n*
0°	—	—	—	—	—	—	—	—	—	—	—	—
−15°	—	—	—	0.8	2	6	1.2	2	6	1.5	2	5
−30°	1.3	2	4	1.5	2	6	—	—	—	1.4	2	4
−45°	0.7	2	4	1.4	2	6	—	—	—	1.3	2	6

Four 4 × 1 linear arrays of differing fixed beam directions are designed to test the azimuth steering capability of the single element. While the element phases can be applied externally, this structure implements the steering internally. A general structure of the four-element linear arrays is shown in Fig. 12. The element spacing (D) is dictated by the via extensions to be 7.2 mm (0.67 λ_o). A transition from GCPW to SIW and a SMP connector are implemented at the feeding port in the simulation models as was the case for the single element. The power is split equally (and with equal phase) through the 1-to-4 splitter. The splitter outputs are coupled to their respective antenna element after passing through passive phase shifters implemented with inductive posts. The splitter and phase shifters are implemented on the top SIW layer, and will thus feed port 1 of each element's polariser.

The intended angles of steering are 0° (element boresight), −15°, −30° and −45°. Table 2 lists the parameter values of the inductive posts in each phase shifter, where a is the post pitch to the SIW wall, p is the posts' pitch to one another and n is the number of posts. Dashes indicate absence of posts.

The larger-than-$\lambda/2$ element spacing will result in grating lobes appearing when steering the array; however, the angle at which they appear will not limit our intended operation. Given the element spacing chosen, the grating lobes will appear when the beam is steered to ±30°; however, they are not expected to be considerable in size (within 3 dB of the main beam) until steered further beyond that angle. This is seen when considering the following equation:

$$\theta = \sin^{-1}\left(\frac{\lambda_o}{D} - 1\right) \tag{3}$$

where θ is the steering angle.

5 Measurement

Prototypes of the single element and four-element arrays are manufactured using the substrate mentioned previously. RO4450T bondply (ϵ_r = 3.35) is used to bond the different layers within the

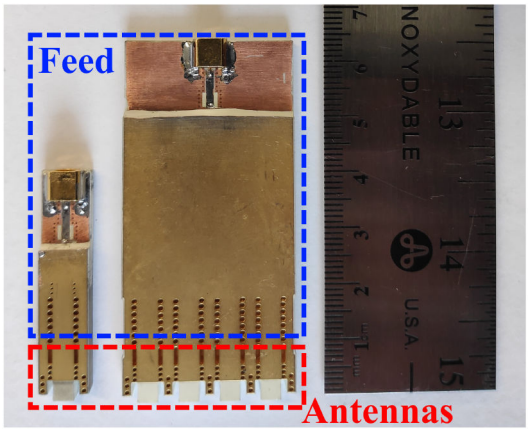

Fig. 13 *Photograph of a single-element prototype and one of the four-element array prototypes*

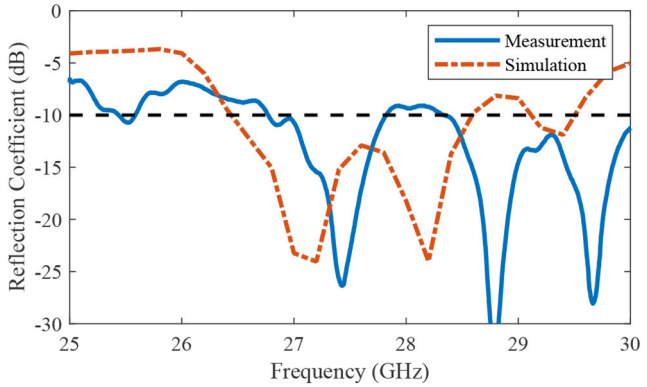

Fig. 14 *Measured and simulated reflection coefficients of a single-element antenna*

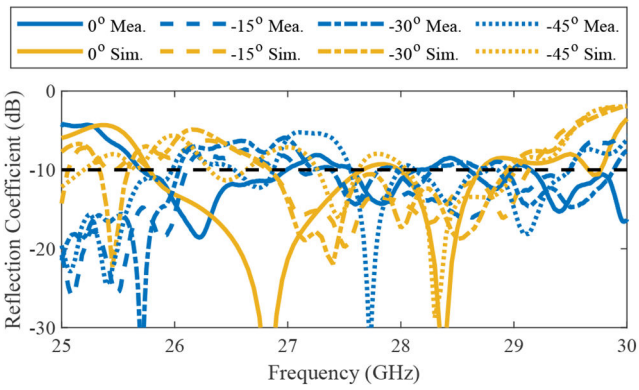

Fig. 15 *Measured and simulated reflection coefficients of* 4×1 *arrays (steered to* $0°$, $-15°$, $-30°$ *and* $-45°$ *in azimuth)*

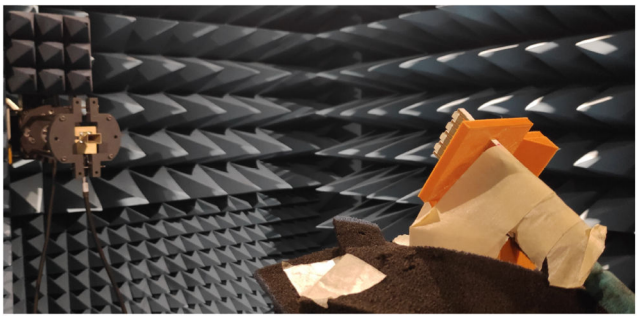

Fig. 16 *Radiation measurement setup*

structure. It is recommended by the manufacturer due to its compatibility with RO4350B, and due to its ideal performance in multi-layer structures (reduced reflow after curing). Despite the higher resin content of RO4450T compared to other bondply materials (thus a greater thickness variation of $\pm 15\,\mu$m), we have not seen, in simulations, discernable variations in impedance matching bandwidth, gain or axial ratio (<60 MHz, <0.13 dB, and <0.9 dB, respectively). Thus, any difference between simulation and measurement is unlikely to be due to the bondply layers. As discussed, a GCPW-to-SIW transition allows coupling to a surface-mounted SMP connector. A single-element prototype and one of the four-element array prototypes are shown in Fig. 13.

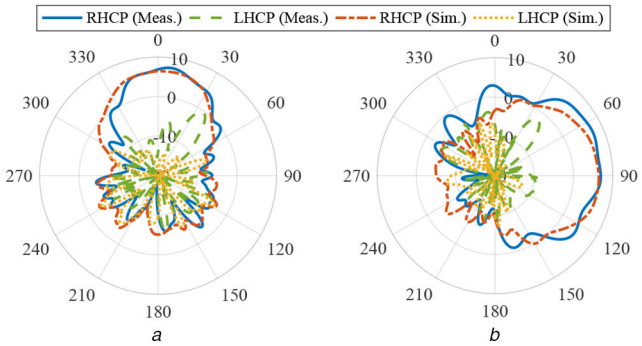

Fig. 17 *Measured and simulated radiation patterns of a single-element antenna at centre frequency*
(a) Azimuth, ***(b)*** Elevation

5.1 Reflection coefficient

Fig. 14 shows the measured and simulated reflection coefficients of the single-element antenna. They are similar, but not in full agreement. The simulated and measured impedance matching bandwidths are 7.1% (26.5–28.5 GHz) and 11.4% (26.7–30 GHz), respectively. The measured bandwidth includes a small increase to -9 dB at 28.2 GHz.

Measured and simulated reflection coefficients of the four arrays are shown in Fig. 15. There are variations between the four arrays, which can be attributed to the different passive phase shifters used. In the simulation, wide bandwidths are seen, especially for the $-15°$ and $-30°$ steering arrays. Similar performances are seen in measurement, with a +300 MHz shift (as was seen for the single-element antenna). These shifts are likely due to differences of ϵ_r at 28 GHz from the datasheet value for 10 GHz.

5.2 Single-element antenna radiation patterns

The RHCP and left-handed CP (LHCP) radiation patterns of the single-element antenna and arrays are measured in an NSI-MI anechoic chamber (with standard gain probes) while mounted on 3D-printed holders. Measurements are taken in the azimuth and elevation planes (of the main beam). A typical measurement setup is shown in Fig. 16.

The measured and simulated radiation patterns of the single-element antenna (in both planes) are shown in Fig. 17. A maximum RHCP gain of 6.3 dBi is achieved in simulation and measurement. An azimuth half-power beamwidth (HPBW) of 60° is achieved in simulation, while it is slightly narrower in measurement. The radiation beamwidths are wide enough in the azimuth plane for wide azimuth steering when using it in an array. In the elevation plane, simulated and measured HPBWs of 75° and 95° are observed, respectively. Knowing that a cross-polarisation discrimination of > 15 dB indicates an axial ratio of better than 3 dB, an azimuth 3 dB axial ratio beamwidth of 75° is achieved in simulation. In measurement, it is a narrower 60°, due to the spike in LHCP gain at 40°. In the elevation plane, a simulated and measured 3 dB axial ratio beamwidth of 115° and 90° are observed, respectively. Thus, within the azimuth and elevation HPBWs, the beam demonstrates CP. Considering non-idealities due to manufacturing and mounting in the chamber (including holders and cable effects), the simulation and measurement results are in good agreement.

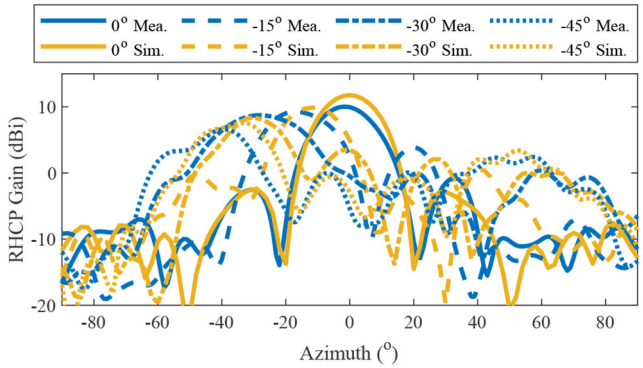

Fig. 18 *Measured and simulated azimuth radiation patterns of four* 4×1 *arrays (steered to* $0°$, $-15°$, $-30°$ *and* $-45°$ *in azimuth) at centre frequency*

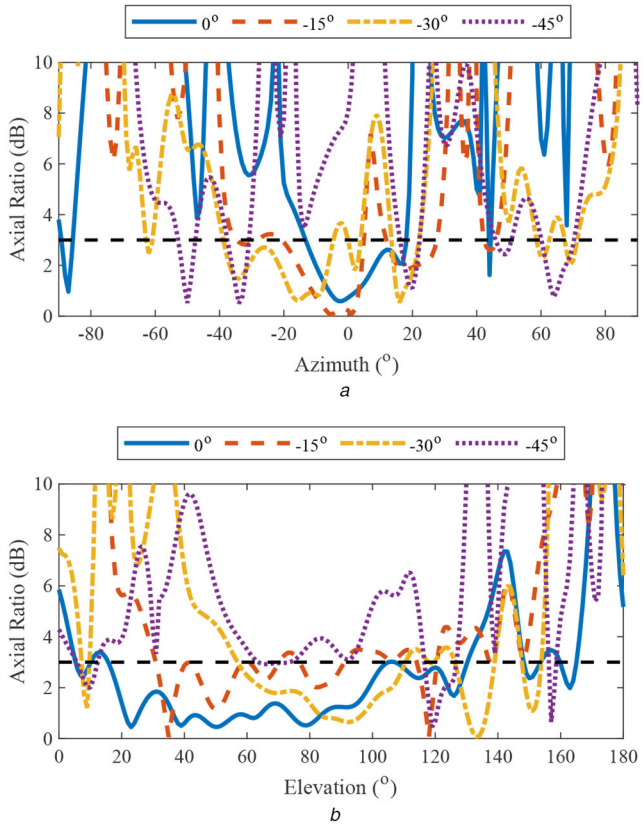

Fig. 19 *Measured axial ratio patterns of four* 4×1 *arrays at centre frequency*
(a) Azimuth, ***(b)*** Elevation

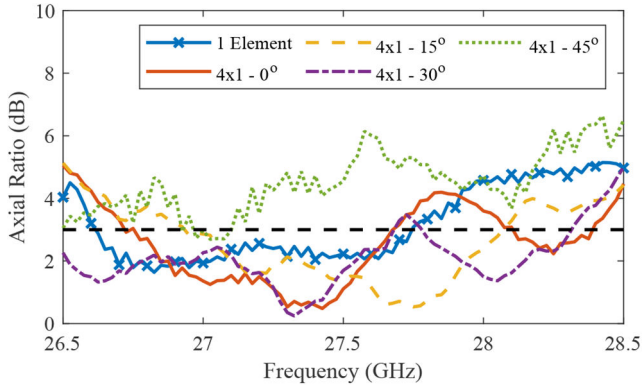

Fig. 20 *Measured axial ratio of a single-antenna element and four* 4×1 *arrays versus frequency*

5.3 Four-element arrays radiation patterns

The radiation properties of the four 4×1 arrays were measured in a similar setup to that of the single-element antenna. The measured and simulated azimuth radiation patterns are shown in Fig. 18. Simulated and measured maximum gains of 11.5 and 10.5 dBi are achieved for the $0°$ array, respectively. The gain is ~ 5 dB greater than that of the single element. A similar maximum gain is observed for the $-15°$ array, while the maximum gain for the $-30°$ array is 8.4 dBi. A maximum gain of 6.9 dBi is achieved with the $-45°$ array, indicating a maximum gain variation of 4 dB. An average azimuth HPBW of $20°$ is achieved in simulation and measurement for all arrays. This beamwidth is expected given the single element HPBW of $60°$ and the number of elements in this array. While grating lobes appear in simulation and measurement for the $-30°$ array, both are seen to be -8.4 dB relative to the main beam. The simulated and measured grating lobes for the $-45°$ array are observed to be within 5 dB of the main beam.

The measured axial ratio patterns are shown in Fig. 19. Azimuth 3 dB axial ratio beamwidths of $36°$, $40°$ and $35°$ are achieved for the $0°$-, $-15°$-, and $-30°$-steering arrays, respectively. The $-45°$ array, however, shows a spike to 5 dB at its respective beam direction. In the elevation plane, measured axial ratio beamwidths of $125°$, $90°$, $80°$, and $40°$ are observed for the $0°$-, $-15°$-, $-30°$-, and $-45°$-steering arrays, respectively. Here a bump to 4 dB at $85°$ is observed for the $-45°$ array.

Fig. 20 presents the axial ratio (at boresight) versus frequency performance of the four 4×1 arrays (and the single-element antenna). It is observed that with the exception of the $-45°$-steered array, wide 3 dB axial ratio bandwidths are achieved. The single-element antenna demonstrates a bandwidth of 1.2 GHz. The $0°$- and $-15°$-steered arrays achieve 1 GHz axial ratio bandwidths, while the $-30°$-steered array's bandwidth is > 1.2 GHz.

By testing the array at different steering angles, we examine the single element's capability to operate in an end-fire beam-steering system. Measured results for steering up to $-30°$ are ideal. Beams within this range demonstrate gains with (at most) 2 dB variance, suggesting that the array could be steered further before a 3 dB gain drop is observed. Within this range, proper axial ratio and radiation beamwidth matchings are observed, indicating clean CP. Azimuth beamwidths increase slightly as the beam is steered. Given the symmetry of the array, and based on interpolation from the measured gain and axial ratio results, the single-element antenna is expected to perform adequately for steering up to $\pm 35°$. Within this range, the gain varies by 3 dB at most, and the axial ratio is better than 3 dB. Employing such an array (with beam-steering mechanism) on the four edges of a mobile device, alongside planar arrays, is a viable option for beam-steering for 5G mobile devices.

This work is compared to other millimetre wave (mmWave) end-fire arrays in Table 3. The work presented in [15] allows for linear and CPs; however, it requires four times as many elements in an array, has a smaller impedance matching bandwidth and smaller gain per element. While larger impedance matching bandwidths and gains are demonstrated in [14, 19], and smaller dimensions are demonstrated in [35, 36], these arrays lack CP and would thus exhibit polarisation loss during most cases of operation. The closest performing structures are those presented in [34, 37]. However, the structure presented in [34] achieves a narrower impedance matching bandwidth and also a poorer 3 dB axial ratio steering range of $\pm 25°$ (despite its wide $\pm 37°$ steering range with 3 dB gain variance). Its larger demonstrated gain of 11 dBi is resultant from its narrower elevation HPBW of $70°$. Furthermore, the structure presented in this study achieves a better radiation efficiency of 69% (compared to 50% in [34]). While the structure in [37] achieves similar performances with identical dimensions (taking into account array size) as our work, the additional need for metal machining downplays the benefit of SIW for PCB manufacturing process integration. This added complexity is also demonstrated in [15, 35] with the need for metal machining and a plastic enclosure, respectively. The slightly reduced radiation efficiency of our proposed array is as a result of losses from the splitter (the single-element antenna radiation efficiency is 79%)

Table 3 Comparisons of different end-fire arrays operating in mmWave

Ref.	Array size, $W \times L \times H$ (λ_0^3)	Structure	Polarisation	Gain steering range	3 dB AR steering range	f_c, GHz	Bandwidth, %	Maximum gain, dBi	Element elevation HPBW, °	Maximum radiation efficiency
[14]	4×1, 2.4 × 0.9 × 0.2	SIW, metasurface	linear	±38°	0°	32.7	37.0	13.8	79	N.I.
[15]	16×1, 3.4 × 0.5 × 0.1	Yagi-Uda & metal machining	linear, CP	N.I.[a]	N.I.	28	7.1	10	N.I.	N.I.
[19]	8×1, 6.1 × 1.2 × 0.5	magneto-electric (ME)-dipole	dual linear	±25°	0°	V: 59.3 H: 58.5	V: 20.9 H: 17.8	V: 16.1 H: 15.1	90	82%
[34]	4×1, 2.3 × 0.8 × 0.7	SIW	CP	±37°	±25°	60	7.8	11.0	70	50%
[35]	4×1, 2.1 × 0.6 × 0.4	Vivaldi	linear	±25°	0°	27.5	18.1	7	N.I.	N.I.
[36]	4×1, 2.0 × 0.2 × 0.1	folded slot	linear	±45°	0°	38.4	9.8	7.7	190	>81%
[37]	8×1, 4.3 ×>0.3 × 0.8	SIW, dipole and metal machining	CP	±35°	±35°	63.9	26	15.3	90	>90%
this work	4×1, 2.9 × 0.8 × 0.3	SIW	CP	±35°	±35°	28	11.4	10.5	95	69%

[a]No information

and a feed that is lossy. While an SMP-to-waveguide transition at the input would greatly improve radiation efficiency (as shown in [37]), it does so at the expense of integration with other components of a standard mobile device. In a realistic implementation, an SMP connector would not be necessary. Furthermore, the splitter could be implemented as a GCPW splitter, with a less lossy GCPW-to-SIW design to the SIW antennas. Therefore, the single-element antenna and arrays presented in this study present desirable performance, without sacrificing size nor compatibility with standard PCB processes, compared to the other works listed.

6 Conclusion

A novel SIW-based CP end-fire antenna has been designed and manufactured. The antenna consists of a notched-septum polariser embedded between two rectangular SIWs, a dielectric lens, and via extensions. The dielectric lens serves to improve radiation patterns and CP purity, while the via extensions are implemented to suppress coupling between adjacent elements when used in an array. The via extensions also serve to improve the front-to-back ratio and the axial ratio of the single-element antenna. The antenna has been implemented in four different four-element arrays with splitters and passive phase shifters. The arrays are used to test the element's steering capability. The measured impedance bandwidth is 11.4%. The measured element gain is 6.3 dBi, while the measured array gains vary from 10.5 to 6.9 dBi depending on beam direction. CP purity within the radiation HPBWs is achieved in azimuth and elevation planes.

Given the ±35° azimuth steering range demonstrated, the antenna's compatibility with (and resilience to tolerances of) standard PCB process and its low profile, the antenna is expected to be a strong candidate for beam-steering mmWave systems. More importantly, this antenna can be used in end-fire arrays, in conjunction with planar arrays, for 3D beam coverage in 5G mobile devices.

7 Acknowledgments

This work was made possible by funding from the Natural Sciences and Engineering Research Council (NSERC), CAD tools access through CMC Microsystems, and dielectric substrates from Rogers Corporation. The authors thank Dr Ashwin Iyer for providing access to the anechoic chamber, and Braden Smyth and Stuart Barth for assistance in operating it.

8 References

[1] Huawei: '5g: A technology vision (white paper)', Huawei, 2013, Available at http://www.huawei.com/5gwhitepaper/

[2] Park, Y.: '5G vision and requirements of 5G forum'. Korea, 2014. Available at https://www.itu.int/dms_pub/itu-r/oth/0a/06/R0A0600005F0001PDFE.pdf

[3] Rappaport, T.S., Sun, S., Mayzus, R., *et al.*: 'Millimeter wave mobile communications for 5G cellular: it will work!', *IEEE Access*, 2013, **1**, pp. 335–349

[4] Boccardi, F., Heath, R.W., Lozano, A., *et al.*: 'Five disruptive technology directions for 5G', *IEEE Commun. Mag.*, 2014, **52**, (2), pp. 74–80

[5] Federal Communication Commission: 'Use of spectrum bands above 24 GHz for mobile radio services; proposed rules', *Federal Register*, 2016, **81**, (8), pp. 1802–1849. Available at https://www.gpo.gov/fdsys/pkg/FR-2016-01-13/pdf/2015-31852.pdf

[6] Hong, W., Baek, K.H., Lee, Y., *et al.*: 'Study and prototyping of practically large-scale mmwave antenna systems for 5G cellular devices', *IEEE Commun. Mag.*, 2014, **52**, (9), pp. 63–69

[7] Ojaroudiparchin, N., Shen, M., Pedersen, G.F.: 'Design of vivaldi antenna array with end-fire beam steering function for 5G mobile terminals'. 2015 23rd Telecommunications Forum Telfor (TELFOR), Belgrade, Serbia, 2015, pp. 587–590

[8] Cheon, Y., Kim, Y.: 'Millimeter-wave phased array antenna with wide beam coverage'. 2016 10th European Conf. on Antennas and Propagation (EuCAP), Davos, Switzerland, 2016, pp. 1–3

[9] El-Halwagy, W., Mirzavand, R., Melzer, J., *et al.*: 'Investigation of wideband substrate-integrated vertically-polarized electric dipole antenna and arrays for mm-wave 5G mobile devices', *IEEE Access*, 2017, **PP**, (99), pp. 1–1

[10] Qiu, Y., Honari, M.M., Ghaffarian, M.S., *et al.*: 'Design and fabrication of non-planar yagi-uda antennas based on a partially conductive filling method', *IEEE Antennas Wirel. Propag. Lett.*, 2019, **18**, pp. 2439–2443

[11] Li, Y., Luk, K.M.: 'A multibeam end-fire magnetoelectric dipole antenna array for millimeter-wave applications', *IEEE Trans. Antennas Propag.*, 2016, **64**, (7), pp. 2894–2904

[12] Hong, W., Baek, K., Kim, Y.G., *et al.*: 'mmWave phased-array with hemispheric coverage for 5th generation cellular handsets'. The 8th European Conf. on Antennas and Propagation (EuCAP 2014), The Hague, Netherlands, 2014, pp. 714–716

[13] Mahmoud, K.R., Montaser, A.M.: 'Design of dual-band circularly polarised array antenna package for 5 g mobile terminals with beam-steering capabilities', *IET Microw. Antennas Propag.*, 2018, **12**, (1), pp. 29–39

[14] Li, T., Chen, Z.N.: 'Wideband substrate-integrated waveguide-fed endfire metasurface antenna array', *IEEE Trans. Antennas Propag.*, 2018, **66**, (12), pp. 7032–7040

[15] Hong, W., Ko, S.T., Lee, Y., *et al.*: 'Compact 28 GHz antenna array with full polarization flexibility under yaw, pitch, roll motions'. 2015 9th European Conf. on Antennas and Propagation (EuCAP), Lisbon, Portugal, 2015, pp. 1–3

[16] Ahmad, Z., Hesselbarth, J.: 'Circuit-board edge-mount dual-polarized millimeter-wave antenna'. 2017 IEEE Int. Symp. on Antennas and Propagation USNC/URSI National Radio Science Meeting, San Diego, CA, 2017, pp. 1443–1444

[17] Ding, K., Gao, C., Wu, Y., *et al.*: 'Dual-band and dual-polarized antenna with endfire radiation', *IET Microw. Antennas Propag.*, 2017, **11**, (13), pp. 1823–1828

[18] Fang, R.Y., Liu, C.F., Wang, C.L.: 'Compact and broadband CB-CPW-to-SIW transition using stepped-impedance resonator with 90°-bent slot', *IEEE Trans. Compon. Packag. Manuf. Technol.*, 2013, **3**, (2), pp. 247–252
[19] Li, A., Luk, K., Li, Y.: 'A dual linearly polarized end-fire antenna array for the 5G applications', *IEEE Access*, 2018, **6**, pp. 78276–78285
[20] Li, A., Luk, K.M.: 'A wideband dual-polarized end-fire antenna array with a single-layer feed method'. 2019 IEEE Int. Symp. on Antennas and Propagation USNC/URSI National Radio Science Meeting, Atlanta, GA, 2019
[21] Cao, Y., Cai, Y., Wang, L.*, et al.*: 'A review of substrate integrated waveguide end-fire antennas', *IEEE Access*, 2018, **6**, pp. 66243–66253
[22] Chen, M., Tsandoulas, G.: 'A wide-band square-waveguide array polarizer', *IEEE Trans. Antennas Propag.*, 1973, **21**, (3), pp. 389–391
[23] Angevain, J.C., Fonseca, N.J.G.: 'Waveguide septum polarizer shaped with legendre polynomials'. 2017 11th European Conf. on Antennas and Propagation (EUCAP), Paris, France, 2017, pp. 2286–2290
[24] Wang, X., Huang, X., Jin, X.: 'Novel square/rectangle waveguide septum polarizer'. 2016 IEEE Int. Conf. on Ubiquitous Wireless Broadband (ICUWB), Nanjing, China, 2016, pp. 1–4
[25] Toyama, N.: 'A cross-shaped horn and a square waveguide polarizer for a circularly polarized shaped beam antenna for a broadcasting satellite'. 1980 IEEE MTT-S Int. Microwave symposium Digest, Washington, DC, 1980, pp. 299–301
[26] Hwang, S.M., Kim, J.M., Lee, K.H.: 'Study on design parameters of waveguide polarizer for satellite communication'. 2012 IEEE Asia-Pacific Conf. on Antennas and Propagation, Singapore, Singapore, 2012, pp. 153–154
[27] Cassivi, Y., Perregrini, L., Arcioni, P.*, et al.*: 'Dispersion characteristics of substrate integrated rectangular waveguide', *IEEE Microw. Wirel. Compon. Lett.*, 2002, **12**, (9), pp. 333–335
[28] Cai, Y., Zhang, Y., Qian, Z.*, et al.*: 'Compact wideband dual circularly polarized substrate integrated waveguide horn antenna', *IEEE Trans. Antennas Propag.*, 2016, **64**, (7), pp. 3184–3189
[29] Esquius-Morote, M., Fuchs, B., Zürcher, J.F.*, et al.*: 'A printed transition for matching improvement of SIW horn antennas', *IEEE Trans. Antennas Propag.*, 2013, **61**, (4), pp. 1923–1930
[30] Esquius-Morote, M., Fuchs, B., Zürcher, J.F.*, et al.*: 'Novel thin and compact h-plane SIW horn antenna', *IEEE Trans. Antennas Propag.*, 2013, **61**, (6), pp. 2911–2920
[31] Cai, Y., Qian, Z.P., Zhang, Y.S.*, et al.*: 'Bandwidth enhancement of SIW horn antenna loaded with air-via perforated dielectric slab', *IEEE Antennas Wirel. Propag. Lett.*, 2014, **13**, pp. 571–574
[32] Cai, Y., Qian, Z., Zhang, Y.*, et al.*: 'A compact wideband SIW-fed dielectric antenna with end-fire radiation pattern', *IEEE Trans. Antennas Propag.*, 2016, **64**, (4), pp. 1502–1507
[33] Wang, H., Fang, D.G., Zhang, B.*, et al.*: 'Dielectric loaded substrate integrated waveguide (SIW) *H*-plane horn antennas', *IEEE Trans. Antennas Propag.*, 2010, **58**, (3), pp. 640–647
[34] Cheng, X., Yao, Y., Tomura, T.*, et al.*: 'A compact multi-beam end-fire circularly polarized septum antenna array for millimeter-wave applications', *IEEE Access*, 2018, **6**, pp. 62784–62792
[35] Kurvinen, J., Kahkonen, H., Lehtovuori, A.*, et al.*: 'Co-designed mmWave and LTE handset antennas', *IEEE Trans. Antennas Propag.*, 2019, **67**, (3), pp. 1545–1553
[36] Park, J., Seong, H., Whang, Y.N.*, et al.*: 'Energy-efficient 5G phased arrays incorporating vertically polarized endfire planar folded slot antenna for mmwave mobile terminals', *IEEE Trans. Antennas Propag.*, 2020, **68**, (1), pp. 230–241
[37] Ruan, X., Chan, C.H.: 'An endfire circularly polarized complementary antenna array for 5 g applications', *IEEE Trans. Antennas Propag.*, 2020, **68**, (1), pp. 266–274